ACS OMEGA

http://pubs.acs.org/journal/acsodf

Article

Hydrothermal Microwave-Assisted Fabrication of Nanohydroxyapatite Powder and Optimization of Its Nanocomposite Coatings on Magnesium Alloy for Orthopedic Applications

Fakiha El-Taib Heakal,* Yahia B. Sarhan, Maamoun A. Maamoun, Amira M. Bakry, Yasser K. Abdel-Monem, and Ibrahim M. Ghayad

Cite This: *ACS Omega* 2022, 7, 1021−1034

Read Online

ACCESS | Metrics & More | Article Recommendations | Supporting Information

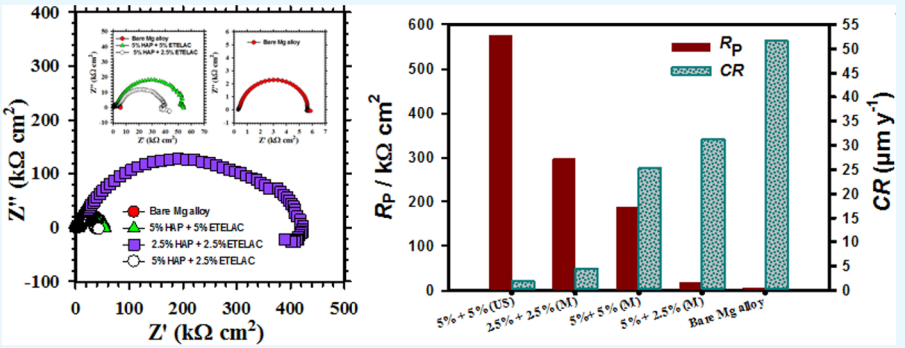

ABSTRACT: Developing appropriate protecting coatings for Mg alloy applications is a challenging issue. Herein, nanohydroxyapatite (nanoHAP) powder was first fabricated by the simple hydrothermal microwave-assisted method. A direct current electrophoresis deposition (EPD) of nanoHAP composite coatings on Mg−3Zn−0.8Ca magnesium alloy was successfully executed. Three suspensions with HAP-dispersive resin solution (ETELAC) ratios (in wt %) of 5−5, 5−2.5, and 2.5−2.5 were chosen for optimizing the effect of applied voltage, deposition time, and stirring mode and rates on the EPD process. NanoHAP composite coatings were applied on each sample in single- and double-run depositions. The results revealed that the maximum weight gain on the coated samples was obtained in 5−5 suspension at 50 V under 150 rpm mechanical stirring rate. Surface examination indicated crack-free coating formation with varying grain sizes. Adhesion tests demonstrated high interconnection between the obtained nanocomposite coatings and the alloy substrate. Electrochemical evaluation measurements in SBF at 37 °C indicated that the corrosion resistance of any coated sample is always superior compared to that of the uncoated bare substrate. It was suggested that the EPD of nanoHAP/ETELAC composite coatings on Mg−Zn−Ca alloy can be a good solution for protecting the alloy from the attack of the aggressive ions bound in the SBF environment.

INTRODUCTION

Implants manufactured from stainless steel,[1] titanium alloys,[2] or polymeric materials[3] exposed patients to a second operation to remove the implants, especially in joining of bone fractures for healing that entails a risk of increasing healthcare costs and delaying the recovery process. Moreover, the difference in hardness between the human bone and the implant might result in osteoporosis. Recently, some polymers and magnesium alloys are considered to be excellent biodegradable implants.[4] But since polymers are expensive and lack the required mechanical strength, magnesium alloys offer a promising alternative to the above materials. Magnesium alloys possess a density of ∼1.74−2.0 g/cm^3, which is close to that of the natural human bone (1.8−2.1 g/cm^3), and their compressive strengths are much higher than those of biodegradable polymers. It is biologically compatible and enhances cell growth and bone formation.[5] However, Mg materials corrode quickly in the presence of chloride ions abound in the physiological fluids, producing magnesium ions and hydrogen gas while shifting the solution pH to higher values.[6]

Received: October 8, 2021
Accepted: December 9, 2021
Published: December 23, 2021

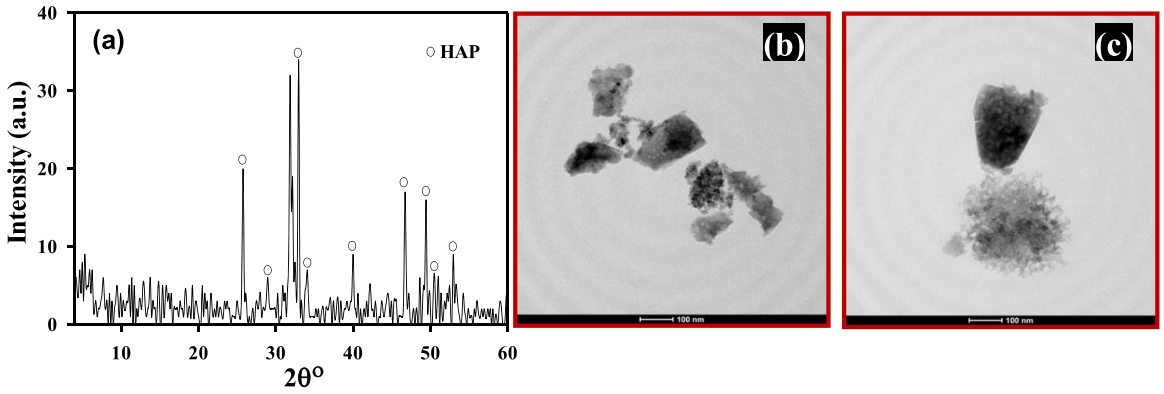

Figure 1. (a) XRD pattern of fabricated HAP and (b, c) two TEM micrographs of as-prepared nanoHAP.

Alloying and coatings are the two main scenarios to overcome these drawbacks. Zn and Ca are two safe alloying elements that act as grain refining and precipitate strengthening agents, hence improving the mechanical properties of magnesium alloys.[7] Zinc can advance the strength of magnesium alloys owing to solid solution strengthening and castability.[8,9] On the other hand, coating has become a powerful alternative tool to protect magnesium materials from corrosion, particularly when utilizing bioactive materials such as hydroxyapatite (HAP) with different forms like particles, films, coatings, and fibers, which have extensive biomedical applications.[10−12] Nanosized HAP powders have a high specific surface area and therefore exhibit enhanced activity toward chemical and biological interactions in the human body. HAP has been known to spontaneously form a bioactive bone-like apatite layer on the bone surface *in vitro* and *in vivo*.[13] HAP has been developed as a coating on metallic implants in the field of orthopedics and dentistry due to its chemical and biological similarity to the human hard tissues as well as direct bonding capability to the surrounding tissues.[14−16] It has been established that HAP coating can promote more rapid fixation and stronger bonding between the host bone and the biomedical implant. Additionally, it provides protection to the implant substrate against corrosion in the biological environment and acts as a barrier against metal ion release from the substrate into the environment. Nevertheless, it lacks the mechanical adhesion with magnesium alloys; therefore, increasing its adhesion is among our targets in the present work. HAP can be deposited by sol−gel,[17] plasma thermal spray,[18] and physical and chemical vapor deposition.[19,20] Electrophoresis deposition (EPD) is a powerful technique for HAP deposition as it is time-saving, cost-effective, and easy to be constructed.[21] Safavi et al. have summarized the major advantages of the EPD technique used for the fabrication of HAP biocoatings.[22] Currently, there is an upsurge of interest in developing high-performance HAP deposits on magnesium alloys. Herein, HAP is electrophoretically deposited on the Mg alloy surface after applying a pretreatment activation step in 40% HF solution to enhance the corrosion resistance and the adhesion of the nanoHAP composite to the magnesium alloy substrate.[23,24] The influence of coating parameters such as applied voltage, deposition time, and agitation was all scrutinized and optimized. Corrosion testing shows that nanoHAP composite coatings on magnesium alloy fabricated by electrophoresis deposition can provide a good corrosion protection for the substrate in simulated body fluid (SBF, pH 7.4), which is used as a corrosive medium at 37 °C.

RESULTS AND DISCUSSION

NanoHAP Powder Characterization. HAP is characterized by a Ca/P atomic ratio of 1.67,[25,26] so it is desirable to maintain this ratio during the fabrication process to achieve a stoichiometric structure of the formed HAP powder. A direct combination of the calcium source with the phosphate source leads to the formation of tricalcium phosphate. EDTA as disodium salt can mask calcium cations, thus preventing them from directly reacting with phosphate anions.[27,28] The process can be simply summarized by eq 1:

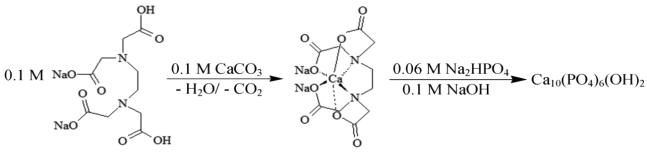

(1)

EDTA as disodium salt is a hexadentate ligand possessing six functional groups, four carboxyl groups, and two amino groups and can be reacted with a divalent cation with an equimolar ratio. It is a good chelating agent for calcium ions, forming several coordination bonds and producing polychelated complexes. The generated very stable five-membered ring complex of Ca^{2+} cations with EDTA would prevent calcium and phosphate ions from directly reacting with each other to form tricalcium phosphate. In the meantime, the calcium carbonate presence helps avoid the formation of a byproduct during the preparation of HAP, where EDTA reacts with an equimolar ratio of $CaCO_3$, forming a stable complex and carbonic acid as a byproduct, which dissociates rapidly, producing water molecules and CO_2 gas. Addition of Na_2HPO_4 as a phosphate ion source together with NaOH as a hydroxide ion source is necessary for the complete formation of calcium hydroxyapatite.[29,30] Basically, the energy of microwave radiations can accelerate the rate of HAP production through a direct interaction of electromagnetic microwave radiations with the polar solvent molecules. This enables water dipoles to absorb radiation, rotate, and gain high enough energy for the formation of HAP.[31]

Figure 1a shows the XRD pattern of the synthesized HAP powder, revealing its crystalline nature. All observed peaks are revised according to a reference code (JCPDS card 01-076-0694), which corresponds to the characteristic chart of calcium hydroxyapatite. As can be seen, the characteristic peaks of HAP

https://doi.org/10.1021/acsomega.1c05625
ACS Omega 2022, 7, 1021−1034

appeared at 2θ positions of 25.7°, 28.9°, 32.8°, 34.1°, 39.9°, 46.6°, 49.5°, 50.5°, and 53.1°, in good agreement with previously reported results,[32,33] which are confirmed by comparing data obtained with those from the International Center for Diffraction Data (ICDD 09-0432) for HAP. NanoHAP is beneficial as an interlocking factor during the healing process after implantation as it increases the mechanical adhesion due to the high increase in the surface area exposed to adhesion.

It can be noted from the transmission electron microscopy (TEM) images in Figure 1b,c that the as-prepared HAP powders are in the nanoscale, where the grain sizes ranged from ∼10 to ∼100 nm, and have almost semispherical shapes. This is consistent with the obtained results from the XRD profile based on the Debye−Scherrer equation.[34]

EPD of the NanoHAP/ETELAC Composite. Based on the zeta potential measurements, the as-prepared nanoHAP particles in aqueous solvent showed negative potential values of −11.4, −11.3, −11.8, and −17.5 mV corresponding to pH values of 5, 7, 9, and 11, respectively. However, the shear plane charge is reversed after thoroughly mixing with ETELAC, giving potential values of +43.6, +52.3, +59.3, and +56.4 mV at pH values of 5, 6, 7, and 8, respectively. Accordingly, deposition of HAP molecules can be easily achieved at the cathode substrate as observed in our experiments. Reversal of the sign of shear plane potential is most likely owing to the electrostatic adsorption of oppositely charged polymer chains on the particle surfaces. Accordingly, it can be proposed that EPD from the currently used suspensions is caused by the electric migration of positively charged ETELAC particles toward the negative electrode (Mg−Zn−Ca alloy). This occurs while dragging the HAP molecules in the same direction.

Prior to each EPD run, the suspension was sonicated for 1 min to obtain a homogeneous dispersion of nanoHAP particles. The sample was visually evaluated after coating, and the weight gain (w_g) was calculated using the following equation:

$$w_g = \frac{w_c - w_o}{A} \quad (2)$$

where w_c and w_o are the weights of coated and uncoated samples, respectively, and A is the sample surface area. Based on preliminary results concerning the properties of turbidity and zeta potential, the most promising suspension was 5% HAP + 5% ETELAC. This suspension has also intermediate conductivity suitable for the electrophoresis process conditions. Therefore, this suspension was selected for carrying out the next experiments.

At each applied voltage, the sample coating was continued until the current has reached a steady value or reduced to zero, indicating no ability for further coating. The sample was then removed from the EPD bath and dried. This run is defined as a single run, which served to determine the minimum current consumed during the formation of the insulating layer. Beyond this current limit, the formed coated layer may be degraded due to the vigorous evolution of hydrogen gas, which leads to the removal or reduction of the coating adhesion to the substrate. The time for each single run is inversely proportional to the applied voltage. At each applied voltage, four samples were coated; the first one represents a single run (S), the second sample was additionally coated for a 5 min double-run experiment (D_5), the third is coated for a 10 min double run (D_{10}), and the fourth one is coated for a 20 min double run (D_{20}). After finishing the coating experiment, each sample was removed from the bath, washed with distilled water, then dried with hot air, and cured in an oven at 130 °C for 30 min. Temperatures higher than 130 °C could cause ETELAC resin decomposition according to the manufacturing company's instructions. The tested experimental parameters that affect the EPD of nanoHAP coatings are the applied voltage, double-run deposition time, suspension concentration, stirring rate, and mode.

Effect of Applied Voltage. The EPD of nanoHAP was established under different applied voltages ranging from 2.5 to 50 V in 5% HAP + 5% ETELAC suspension without stirring and with mechanical stirring at 150 rpm. For the S experiments, the weight gain was estimated as a function of the applied voltage, and the results are summarized in Table S1a,b. Generally, the observed increase in weight gain with the applied voltage of up to 30 or 40 V is likely attributed to the enhancement of the particle average velocity v (m s^{-1}) in the suspension toward the cathode according to the following equation:[35,36]

$$v = \mu E \quad (3)$$

where μ (m^2 s^{-1} V^{-1}) is the electrophoresis mobility and E (V m^{-1}) is the applied electric field. All tested voltages give homogeneous sponge-like deposits from nanoHAP/ETELAC composite coatings.

Under unstirred conditions, at lower voltages of 2.5 and 5 V, the measured currents start at 1 and 2 mA/cm^2 and decrease slowly to zero after 5 and 4 min, respectively, during deposition. The extended deposition periods gave more chance for water molecule electrolysis to generate extra hydrogen gas evolution at the cathode during EPD.[37] This is possibly due to the relative high conductivity of this 5−5 suspension (96 μS/cm). Gas evolution adversely affects coating adhesion as it would hinder the driving force (EMF) necessary to withdrawing HAP particles from the solution toward the cathode,[21] resulting in an inhomogeneous coating on the substrate surface as found experimentally. Upon increasing the applied voltage to 10 V, the start current increases to 2.4 mA/cm^2, while the deposition time decreases to 3 min. The deposition time required for achieving zero current becomes shorter the higher the applied voltage is. This is simply due to the enlargement of the driving force needed to drag the particles from the suspension to the cathode associated with more coatings and consequently with higher resistance to the current passing. Empirically, for the high applied voltages of 15 and 20 V, the deposition currents start at 6 and 8 mA/cm^2 and then fall to zero after 150 and 120 s, respectively. Indeed, the increase in weight gain with increasing applied voltage is consistent with Faraday's first law stating that the weight of reacted or deposited materials is directly proportional to the quantity of charges passing. A higher thickness from the coated layer is obtained at 30 V (Table S1a), mainly because the driving force dragging HAP particles toward the cathode is high enough to neglect the negative impact of water electrolysis. At this voltage, the current starts initially at 16 mA/cm^2 and reaches a steady value of 1 mA/cm^2 after 90 s only. When the applied voltage is further increased to 40 V, the weight gain of the formed coating is markedly decreased, and the starting current amounts to 22 mA/cm^2 and then reduces quickly in 60 s to a steady value of only 2 mA/cm^2. Such decay in the weight is related to the increase in water molecule electrolysis, leading to a coated layer with a

https://doi.org/10.1021/acsomega.1c05625
ACS Omega 2022, 7, 1021−1034

more defective structure due to the excessive gas evolution. The formed gas molecules act also as an insulating layer between the cathode and the deposited particles. A further increase in the applied voltage of up to 50 V leads to a coated layer with bad morphology having more coating-free zones and defects. At 50 V, the current starts at 25 mA/cm^2 and stabilizes at 3.3 mA/cm^2 after 30 s. According to the above S run results, 30 V is considered the optimal applied voltage for nanoHAP/ETELAC composite coating formation.

Under conditions of mechanical stirring at 150 rpm, the result under a low applied voltage of 2.5 V was not good, and thus, it is not included in Table S1b. As can be seen, the weight gain increases with increasing applied voltage until a maximum value at 50 V. However, upon increasing the applied voltage to 75 V, the starting current reported initially at 40 mA/cm^2 diminishes to 4 mA/cm^2 after 20 s only, and a decline in the weight gain is noted. Plainly, this behavior may be related to a decrease in the particles' concentration per unit volume of the suspension adjacent to the cathode due to a high applied electric field. This entails that the rate of particle reduction and deposition becomes higher than the rate of particle migration, a situation that causes a rapid discharge for all particles reaching the cathode, leaving instead water molecules near the electrode surface ready for electrolysis and generation of hydrogen gas. This will spawn a porous-coated layer and lead to a decrease in weight gain value, in compliance with the following Zhitomirsky relation:[38,39]

$$\rho A x = \frac{C \mu U t}{d} \tag{4}$$

where C is the concentration of particles in the suspension, ρ is the apparent density, A is the electrode surface area, x is the deposited layer thickness, μ is the mobility of the particles, $U_{eff} = U_{app} - U_{dop}$ is the effective applied voltage of EPD (U_{dop} being the voltage drop during EPD), t is the deposition time, and d is the distance between the two electrodes. Therefore, it can be concluded that by increasing the EPD voltage, a larger coating thickness (x) and weight gain are realized. Because of this facile formation of the barrier layer, a voltage drop (U_{dop}) takes place in a shorter time, leading to a rapid discount in both values of the effective U and the deposition rate. Hence, applying a high voltage of 75 V is conducive to a bad result depending on this reasonable notion (Figure 2).

Effect of Double-Run Deposition Time. Carrying out deposition experiments as single runs only may not give a satisfactory result. To limit the effect of gas evolution, double runs are suggested at each applied voltage. Drying the sample after each single run removes any embedded gas from the substrate surface, giving a chance for enhanced mechanical adhesion of the coated layer formed during the double-run assembly. Table S2 shows weight gain results at each applied voltage obtained for D_5, D_{10}, and D_{20} experiments without and with mechanical stirring at 150 rpm. Usually, under the unstirred conditions, the results obtained from double runs, even those at the lowest time (D_5), are better compared to their counterpart weight gains from the S runs (Table S1). In the meantime, under unstirred or stirred conditions, the weight gain at any given applied voltage increases with increasing time of the double run from D_5 to D_{20}, but the weight gain and the coating thickness are usually higher in the stirred suspensions compared to the unstirred ones.[37−40] A low applied voltage of 2.5 V does not yield homogeneous deposition, and instead, particle agglomeration has been discerned. Under unstirred conditions, an approximately steady weight gain value is obtained at 30 to 50 V for D_5 experiments, while for D_{10} runs, the maximum weight gain values are obtained at 30 to 40 V and at 40 V for the D_{20} experiments. A further increase in the applied voltage of up to 50 V did not produce an enhanced weight gain due to energetic hydrogen gas evolution, which impedes the particles from reaching the cathode surface.

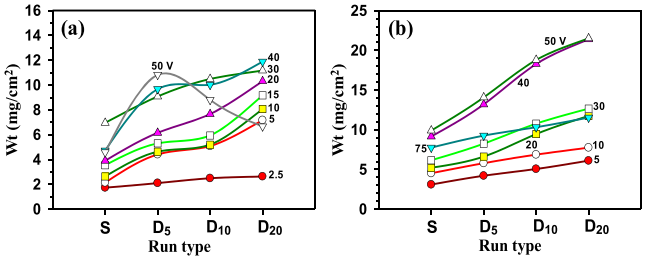

Figure 2. Weight gain as a function of the applied voltage for all runs in 5% HAP + 5% ETELAC suspension: (a) without stirring and (b) with mechanical stirring at 150 rpm.

Results listed in Table S2 disclose also that for all double-run experiments under stirring conditions, weight gain values at an applied voltage of 50 V are always the highest. Continuous stirring of the suspension increases its ability to remove any evolved gases, which would improve the deposition of the formed nanoHAP/ETELAC composite layer on the substrate surface. A further increase in the applied voltage of up to 75 V affects adversely the coating process due to intense energetic gas evolution as mentioned above (Figure 2b).

Effect of Stirring Rate and Mode. As an experimental fact, prepared nanoHAP/ETELAC suspensions are stable for approximately 1 h, which can allow nanocomposite deposition without stirring.[41] On the other hand, the aforementioned results plainly indicate that stirring the suspension increases the weight gain for both S and D runs. When the deposition voltage is increased (more than 30 V) in a stagnant suspension, the obtained final coatings are found to be inhomogeneous and porous owing to the gas evolution during the coating formation process. Stirring the suspension increases the driving forces acting upon the particles, bringing them to the cathode more easily and finally depositing them with the help of the external applied electric field. Figure 2a,b reveals also that a good coating is achieved under mechanical stirring of the solution, and the best result is obtained at 50 V with stirring of the suspension at 150 rpm compared to electrophoresis deposition experiments in the unstirred suspensions.

Different coatings were performed using S runs in 5% HAP + 5% ETELAC suspension at 50 V with different rates of mechanical stirring over the range from 0 to 250 rpm. It can be realized from these results (Table 1) that increasing the stirring rate up to 150 rpm continuously enhances the particle movement in the suspension and affects positively their ability to reach the cathode surface faster, where they deposit there and increase its weight gain. Therefore, a lower stirring rate

Table 1. Weight Gains at Different Rates of Mechanical Stirring for the S Runs in 5% HAP + 5% ETELAC Suspension at 50 V

mechanical stirring rate (rpm)	without	50	100	150	200	250
weight gain (mg/cm^2)	4.58	7.30	8.10	9.90	9.85	9.40

https://doi.org/10.1021/acsomega.1c05625
ACS Omega 2022, 7, 1021−1034

should be avoided, as we require enough driving force to encourage particles to reach the electrode surface. Indeed, mechanical stirring at 150 rpm affords the optimum condition for a sufficient driving force that can effectively push the suspension particles toward the cathode. A high stirring rate more than this threshold value would agitate the suspension particles more rapidly, causing deficiency in their adhesion on the substrate with a subsequent reduction in weight gain as observed in Table 1.

The effect of agitation mode was also explored by performing single S and double D_{20} run experiments at 50 V in 5% HAP + 5% ETELAC suspension using 80 W ultrasonic (US) irradiation power, as well as with mechanical stirring at 150 rpm (Table 2). Experimentally, it was noticed that under US conditions, the deposition current started at 25 mA/cm^2 and decayed to zero after 3 min. Such a long decay time might disperse the particles away from the cathode surface and hence slow down the deposition rate. This would be due to the formation of a microemulsion resulting from the ultrasonic cavitation,[42] albeit ultrasonic waves have the ability to easily evacuate any fast gas evolution during the deposition process. In the case of the D_{20} run, the consumed current never reduces to a zero value; therefore, extending more the deposition time will not produce any improved results.

Table 2. Weight Gain under Ultrasonic Radiation and Mechanical Stirring Conditions in 5% HAP + 5% ETELAC Suspension at 50 V

run type	single S run	double D_{20} run
ultrasonic bath at 80 W	3.74 mg/cm^2	8.29 mg/cm^2
mechanical stirring at 150 rpm	9.90 mg/cm^2	21.52 mg/cm^2

Effect of HAP and ETELAC Concentrations. In this experimental set, the suspension concentration is changed to examine its effect on the weight gain and morphology of the produced nanocomposite coatings and to identify the optimized suspension concentration that gives the best results. For this purpose, two additional concentrations are tested, namely, 5% HAP + 2.5% ETELAC (5−2.5) and 2.5% HAP + 2.5% ETELAC (2.5−2.5) suspensions. The use of 5−2.5 suspension could be beneficial due to its low conductivity amounting to 78 μS/cm, expecting to give a lower extent of water molecule electrolysis. The results of deposited weight gain using this suspension are recorded in Table S3a and presented in Figure 3a. As can be seen, the weight gain increases with increasing applied voltage from 5 to 50 V for the S, D_5, and D_{20} runs in a manner that agrees very well with Faraday's first law. For the S run specifically, a further increase in the applied voltage beyond this limit produces a sudden decrease in the weight gain due to hydrogen gas evolution as mentioned before. However, executing the double runs D_5 and D_{20} at 75 and 100 V offers more driving forces for the suspension particles to elaborate better surface design for the substrate, leading to a thicker layer formation with better homogeneous morphology from nanoHAP/ETELAC composite coatings.

On the other hand, in the more diluted 2.5−2.5 suspension at the lower applied voltages of 5 and 10 V, the weight gain results were too small, and hence, they are not included in Table S3b and Figure 3b. Generally, the weight gains obtained in the dilute suspension are less than their counterparts produced in the two other studied concentrated suspensions, likely due to its lower electrical conductivity being 68 μS/cm. Usually, a low conductivity induces a delay in the suspension response to the applied electric field and thus slows down the deposition rate. Nevertheless, at higher applied voltages, better surface designs and good thinner coatings could be formed for all run types (S, D_5, and D_{20}). Herein also, the weight gain increases at each definite voltage from single S to double D_5 and D_{20} runs and increases as well with increasing applied voltage, consistent with Faraday's first law of electrolysis.

The effect of suspension concentration on the deposition process for the single S run experiments at all applied voltages can be deduced from Figure 4a, which infers that the weight gain increases with the increase in the applied voltage. At 50 V, the weight gain attains its maximum value for both 5−2.5 and 5−5 suspensions, being higher in the former than in the latter. The increase in the weight gain obtained in 5−2.5 suspension confers more surface designs on the substrate. In contrast, weight gain values obtained in 2.5−2.5 suspension are the lowest for the reasons mentioned above. Additionally, in this lower suspension concentration (2.5−2.5), the diffusion layer is relatively thicker and the particles reach their isoelectric point at a longer distance from the substrate surface. This would lead to a reduction in the deposition rate and, consequently, production of a relatively thin coated layer.[43−46] Similar results are observed for the double D_5 and D_{20} runs as shown in Figure 4b,c, respectively. In all studied suspensions with different concentrations, more weight gains

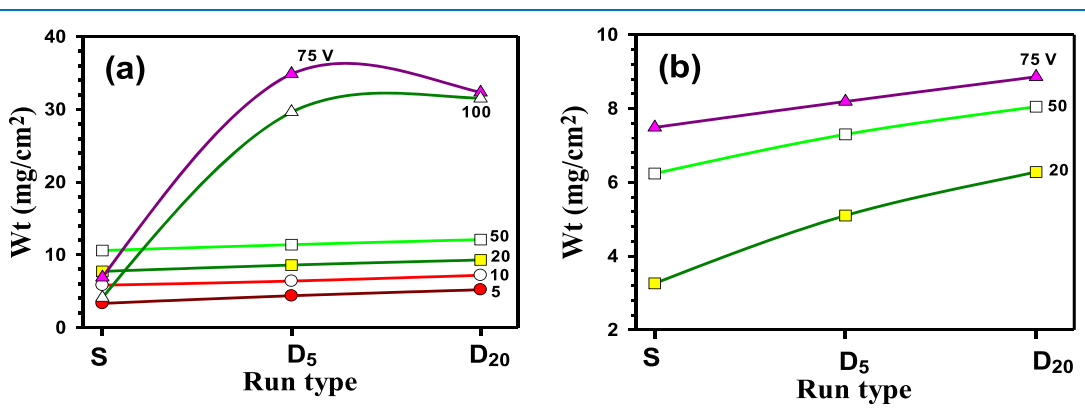

Figure 3. Weight gain as a function of the applied voltage for all runs in (a) 5% HAP + 2.5% ETELAC and (b) 2.5% HAP + 2.5% ETELAC suspensions with mechanical stirring at 150 rpm.

https://doi.org/10.1021/acsomega.1c05625
ACS Omega 2022, 7, 1021−1034

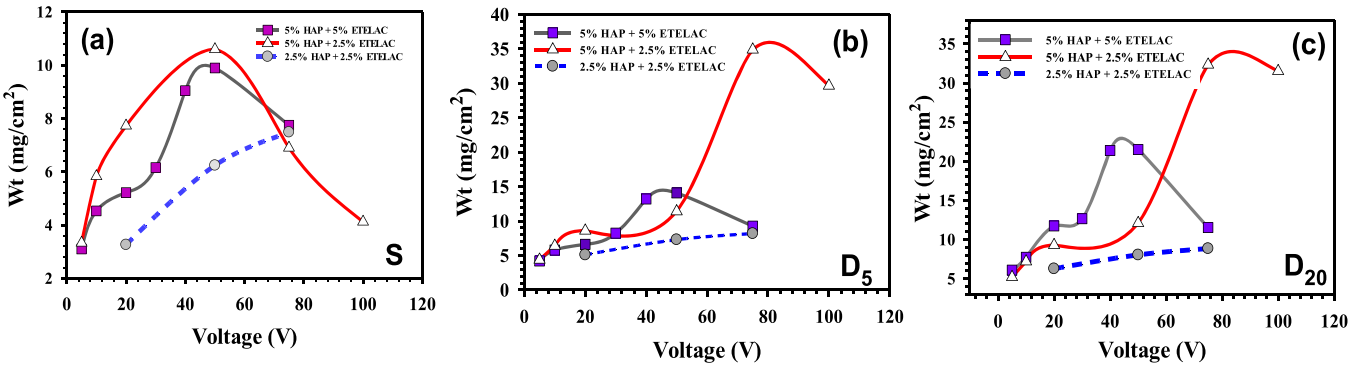

Figure 4. Weight gain against applied voltages for (a) S runs, (b) D_5 runs, and (c) D_{20} runs in the different tested suspensions with mechanical stirring at 150 rpm.

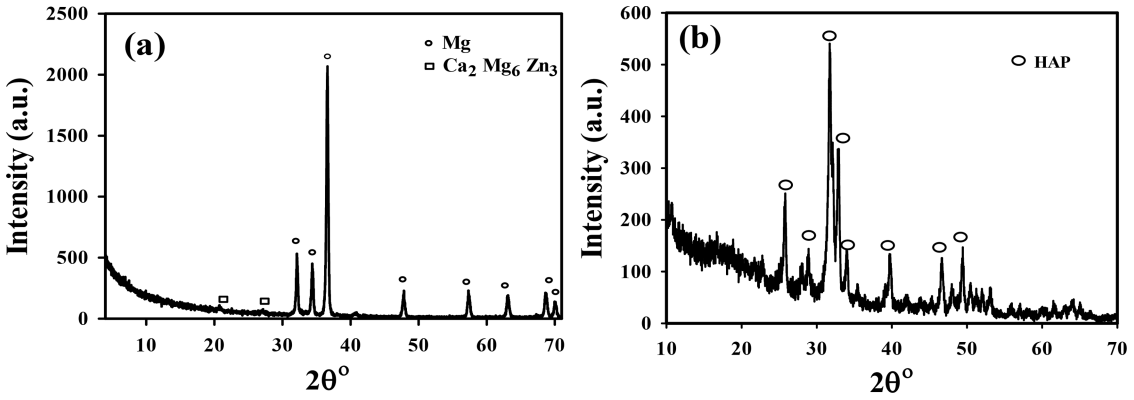

Figure 5. XRD patterns of (a) uncoated and (b) coated alloys (D_{20} run at 50 V in 5−5 stirred suspension at 150 rpm).

are obtained with the extension of the deposition time of the double runs.

Characterization of Nanocomposite Coatings. The XRD pattern of the bare Mg−0.8Ca−3Zn alloy shown in Figure 5a reveals peaks due to Mg and the $Ca_2Mg_6Zn_3$ phase, which is formed at the grain boundaries.[47,48] The observed high intensity of the peaks is obviously related to the high crystallinity of the Mg alloy surface. On the other hand, the XRD pattern of the coated sample in Figure 5b displays peaks due to the base Mg alloy at 2θ positions of 32.1°, 34.3°, and 36.6° that disappear or are attenuated as HAP peaks prevailed. The characteristic peaks that appeared at 2θ of 25.6°, 31.8°, 33.5°, 34.3°, 39.4°, 46.2°, and 49.5° matched well with ICDD 09-0432 for HAP. This indicates that the major phase on the surface is HAP in addition to peaks attributed to the substrate. The intense peak for HAP that appeared at 2θ of 31.81° corresponds to a *d*-value (interplanar spacing) equal to 2.81 Å. The outcome of the XRD data confirms the high efficiency of the coating process and even surface coverage of the magnesium alloy by nanoHAP/ETELAC composite coating.

Figure 6 shows the field emission scanning electron microscopy (FE-SEM) images of the coated samples in the three 5−5, 5−2.5, and 2.5−2.5 suspensions using the D_{20} run at 50 V under stirring conditions. It is obvious that the surface morphology of the sample coated in a 5−5 suspension US bath (Figure 6b) is quite different from the images of the other three samples coated under mechanically stirred conditions. It has almost a thin smooth flattened surface that is widely interrupted, making the underlying darker film clearly visible with a nice spongiform pattern. In Figure 6a,c,d, the gradual increase in the weight gain (mg/cm^2) of the surface coating film results in a gradual increase in the irregular convolution pattern having small voids and pinholes as well: 5−5 (21.52) > 5−2.5 (12.10) > 2.5−2.5 (8.05). This leads to a subsequent decrease in the visibility of the interrupted sites overlying the underlying film, where Figure 6d < Figure 6c < Figure 6a. The energy dispersive X-ray (EDX) results of the same four samples are depicted in Figure 7. Generally, EDX analysis shows a Ca/P wt % ratio of more than 2, which is far from that for the HAP particle ratio. The presence of a relatively high percentage of both C and N atoms coming from the dispersive ETELAC phase indicates the good insertion of ETELAC constituents in the formed composite coating.

EDX analysis presented in Figure 7b discloses high contents from the ETELAC elements than those from the HAP particles. Formation of a crack-free flat spongiform pattern coating can enhance the mechanical interlinking between the coating and the body tissues after a medical implantation. The coated sample in 5−2.5 suspension gives a high percentage of HAP constituents as obtained by its EDX spectra shown in Figure 7c, which can be correlated with the concentration ratio of the suspension. The percentage of both Ca and P is high compared to that of the ETELAC constituents from C, N, and O elements. Moreover, the ETELAC percentage ratio affects the suspension stability by increasing its propensity for agglomeration in agreement with its SEM image. Finally, EDX analysis shown in Figure 7d for the lower suspension concentration (2.5−2.5) specifies a Ca/P ratio different from that in HAP. It is obvious that ETELAC constituents from C and N atoms are higher than HAP constituents from P and Ca. The increase in ETELAC concentration in the formed coated layer increases its compactness. The presence of Mg in the

https://doi.org/10.1021/acsomega.1c05625
ACS Omega 2022, 7, 1021−1034

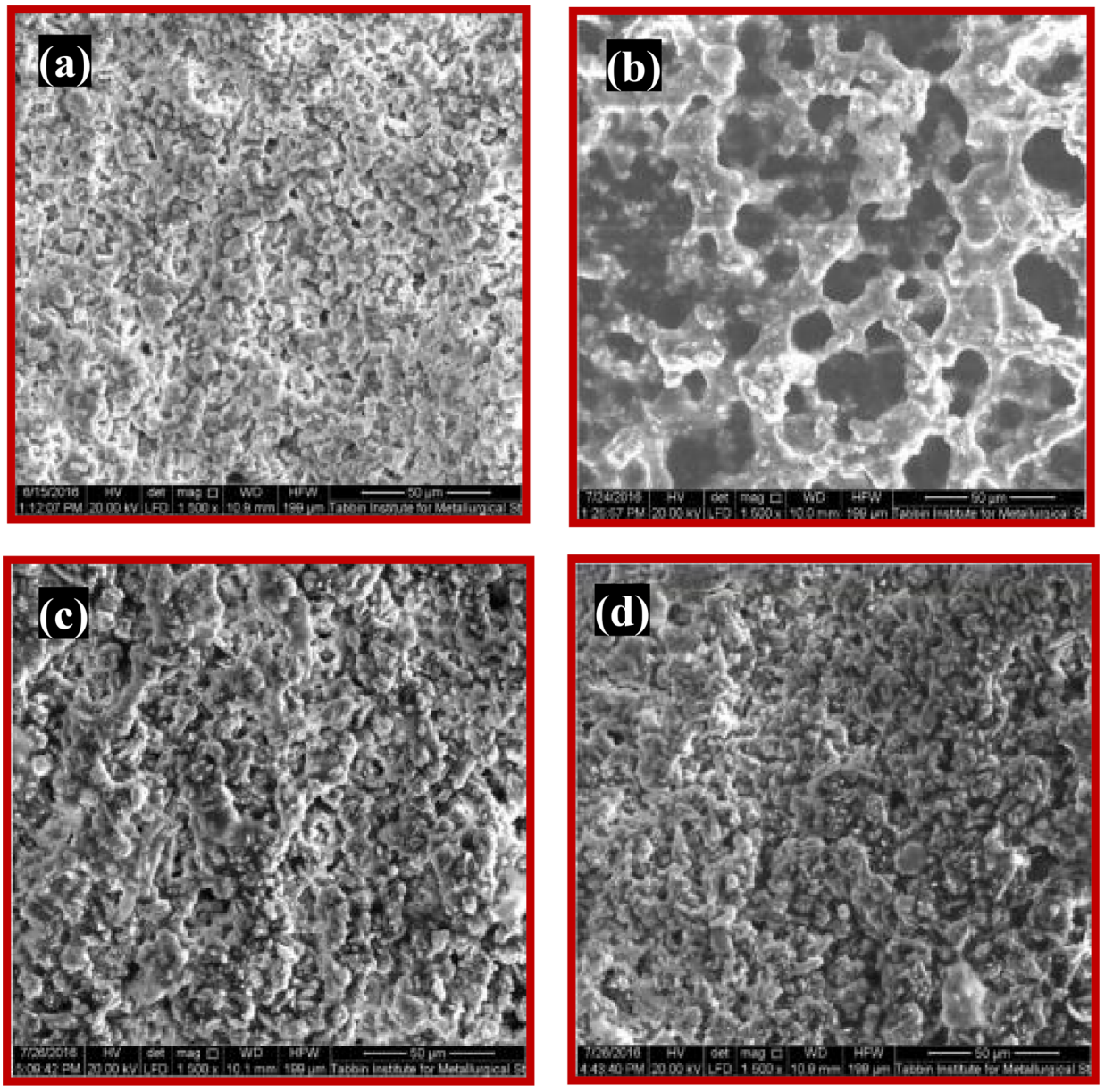

Figure 6. FE-SEM images of Mg alloy samples coated at 50 V in (a) 5−5 suspension mechanically stirred at 150 rpm, (b) 5−5 suspension ultrasonically stirred, and (c) 5−2.5 suspension and (d) 2.5−2.5 suspension both mechanically stirred at 150 rpm.

EDX analysis data may be caused by the presence of some fine pores, which permit a connection to the preformed magnesium fluoride interlayer. It can thus be stated that composite coatings formed by EPD in all tested suspensions have Ca and P percentage ratios arranged in the order 5−2.5 > 5−5 (ultrasonic bath) > 2.5−2.5 > 5−5 and those of C arranged in the order 2.5−2.5 > 5−5 > 5−5 (ultrasonic bath) > 5−2.5.

Adhesion Test. The adhesion strength of a coating can present important information about its mechanical properties, which is considered among the most vital possessions for the *in vivo* implantation. Therefore, it is important to indicate whether the composite coatings have suitable adhesion with its metallic substrate or not. An adhesion test was carried out according to the ASTM D3359 standard test method for measuring adhesion by a tape test.[49,50] This technique can reveal much more about the true adhesion behaviors of a coating system. The obtained results of the adhesion test reveal that all coating layers adhere well with the alloy substrate without any peeling off as shown in Figure 8 with a rating of 5 A. It can be concluded that HAP in ETELAC suspension can produce ceramic coatings with high interfacial bond strength.

Electrochemical Corrosion Behavior Assessment. *Electrochemical Impedance Spectroscopy (EIS).* EIS is one of the most powerful nondestructive techniques for predicting and assessing the corrosion protection efficacy of various coatings based on the ranking of the values of their corrosion resistance during traditional exposure tests.[51,52] Herein, EIS measurements were utilized to study the performance of the prepared coatings under the assayed experimental conditions after 1 h immersion in SBF at 37 °C. The EIS results are depicted in Figure 9a,b as Nyquist and Bode plots for the different coatings formed in the three chosen suspensions. A bare uncoated Mg−Zn−Ca alloy sample is also shown for comparative purposes. As evident from Figure 9a, all coated samples give negative imaginary impedance (Z'') values at the most lower frequency end of the spectra, indicating the

https://doi.org/10.1021/acsomega.1c05625
ACS Omega 2022, 7, 1021−1034

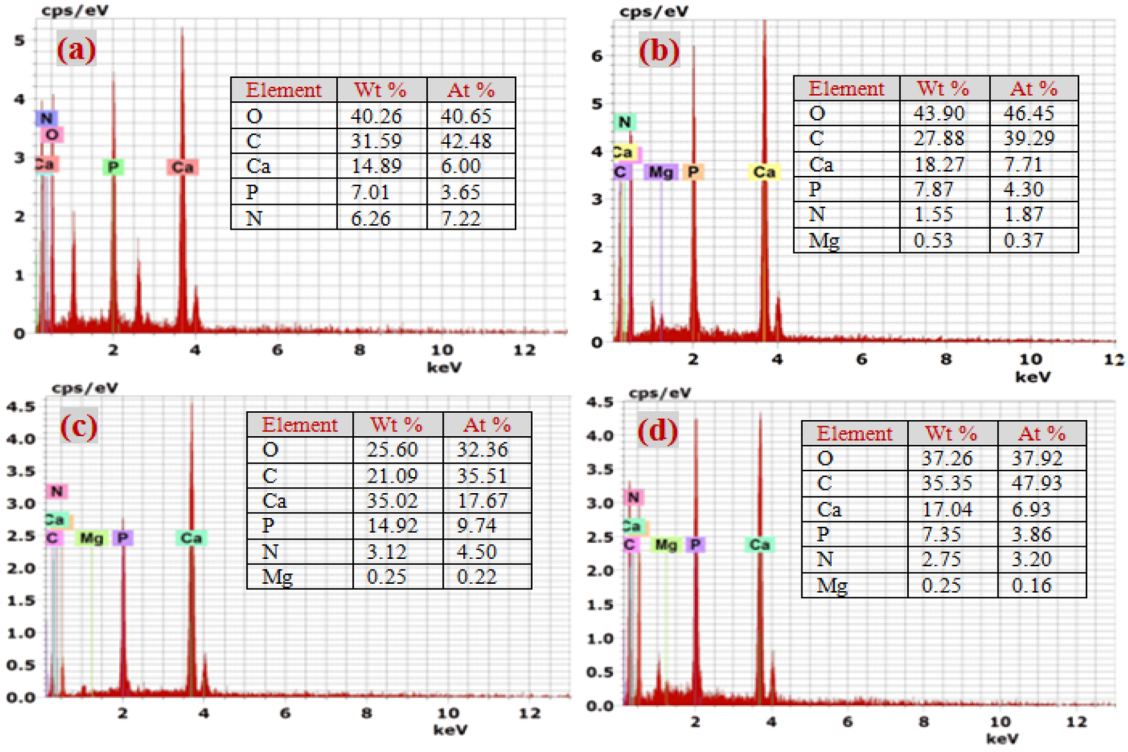

Figure 7. EDX spectra of Mg alloy samples coated at 50 V in (a) 5−5 suspension mechanically stirred at 150 rpm, (b) 5−5 suspension ultrasonically stirred, and (c) 5−2.5 suspension and (d) 2.5−2.5 suspension mechanically stirred at 150 rpm.

presence of inductive properties for the composite coatings, albeit with somewhat low degree compared with the uncoated sample, which confers a better barrier property of the prepared coatings.[53] It is also obvious that the size of the capacitive loop shown in the Nyquist diagram depends seriously on the HAP/ETELAC suspension concentration used to prepare the composite coating. Based on the ASTM standard (G 102-89),[54] the capacitive loops are related to the corrosion behavior and coating capacitance of the sample. Thus, for comparison, one can take the real impedance (Z') of the capacitive loop at a Z'' value equal to zero to be the charge transfer resistance and consider it as a measure of the corrosion resistance (R_{corr}).[55] Accordingly, the impedance of the coated sample obtained using 5−2.5 suspension is equal to 43.350 kΩ cm^2, which increases to 53,802 kΩ cm^2 for the one prepared in 5−5 suspension and further increases significantly by approximately one order of magnitude (418.200 kΩ cm^2) for the coated sample obtained in 2.5−2.5 suspension. The results illustrate clearly that the suspension concentration plays a vital role in the protection performance of the formed composite coating by EPD. With regard to the EDX analysis, the substantial relative increase in the capacitive semicircle loop for the sample coated in 2.5−2.5 suspension is mainly related to the formation of composite coating with high ETELAC content that heightens its insulation properties and greatly ameliorates the corrosion resistance of the coating as mentioned above. In addition, the low frequency region of the Bode plot is dominated by the charge transfer and solution resistance. So, a higher Z modulus value is indicative of a higher corrosion resistance value as the case of all coated samples in comparison with the bare Mg alloy. Briefly, based on the corrosion resistance of the produced coating in SBF solution, the three tested suspensions can be arranged as follows: 2.5−2.5 > 5−5 > 5−2.5 > bare Mg alloy substrate. This ranking discloses that the best stable and protective coating in SBF solution is the one formed on the Mg alloy sample using the lowest concentrated suspension (2.5−2.5).

Moreover, the impact of stirring mode on the impedance behavior of EPD coatings can be disclosed by measuring the EIS spectra in SBF at 37 °C for the uncoated Mg alloy and coated sample prepared in 5−5 suspension at 50 V under either mechanical stirring at 150 rpm or ultrasonic radiation as presented in Figure 10. The spectra on both Nyquist (a) and Bode (b) formats reveal that the coating produced under ultrasonic radiation has a quite large corrosion resistance value compared to its counterpart coating prepared in a mechanically stirred bath at 150 rpm. As can be seen in Figure 10, the real impedance (Z') at the low frequency limit (0.01 Hz) achieves a quite large value of 1000 kΩ cm^2, demonstrating a great improvement in the compactness of the coated layer produced under ultrasonic stirring mode. This behavior is in good agreement with the SEM image morphology and EDX analysis shown in Figures 6b and 7b, respectively.

Potentiodynamic Polarization Measurements. The corrosion behavior of the different tested samples in SBF at 37 °C was also scrutinized using potentiodynamic polarization curves (or Tafel curves, E vs log i plots) as shown in Figure 11a. Analysis of those curves was performed by the extrapolation method in the Tafel region to derive the electrochemical corrosion parameters of the coated samples in comparison with the uncoated bare Mg alloy substrate as summarized in Table 3. Careful inspection of this table and Figure 11a reveals some relevant important inferences concerning the different corrosion traits.

(i) All coated samples exhibited lower i_{corr} values compared to the bare Mg alloy substrate (2.233 μA cm^{-2}). (ii) Under the same conditions of both applied voltage (50 V) and mechanical stirring (MS at 150 rpm), the lowest i_{corr} value of

https://doi.org/10.1021/acsomega.1c05625
ACS Omega 2022, 7, 1021−1034

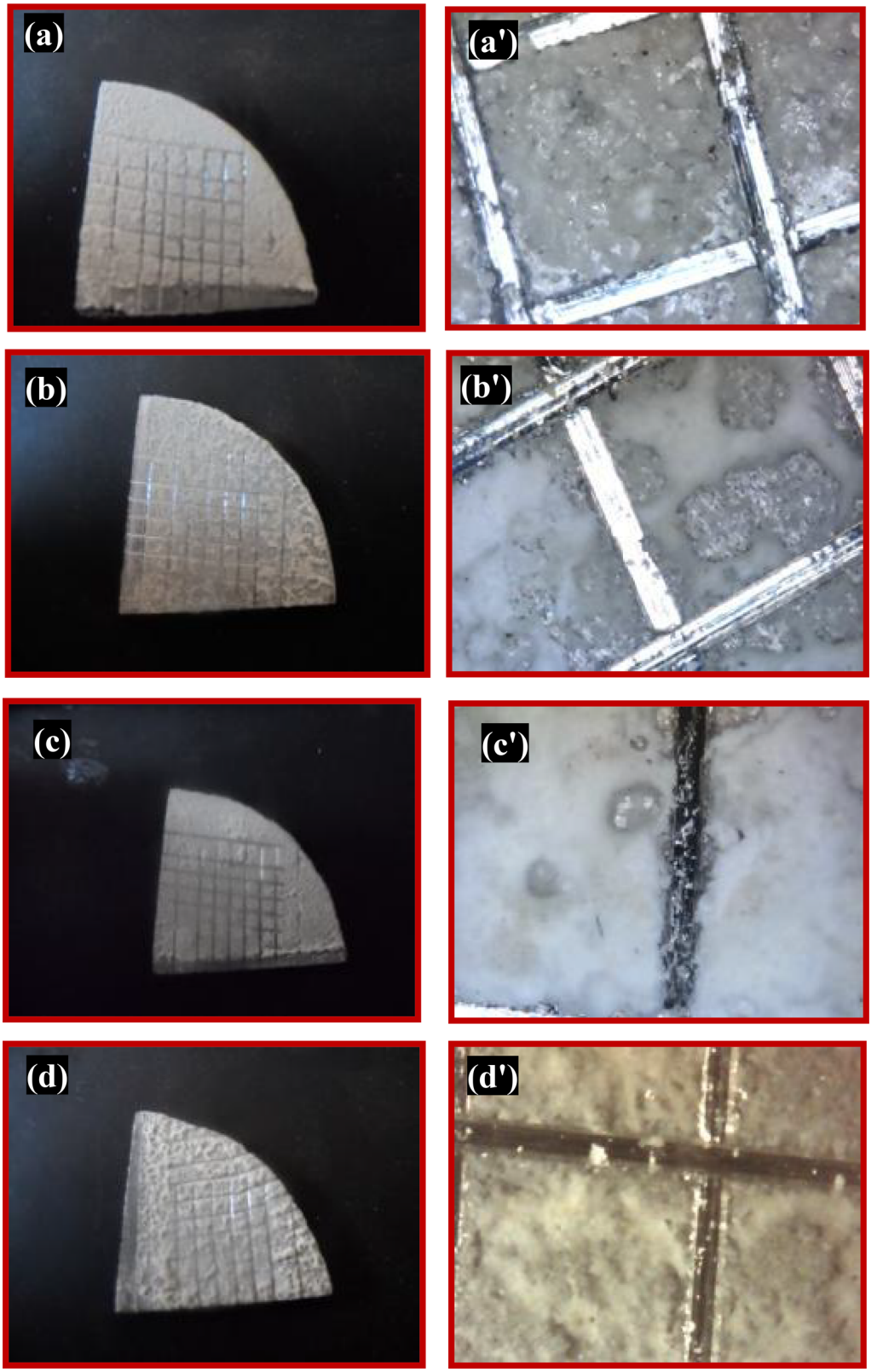

Figure 8. Images after the adhesion test of EPD-coated Mg alloy samples at 50 V in (a, a′) 5−5 suspension mechanically stirred at 150 rpm, (b, b′) 5−5 suspension ultrasonically stirred, and (c, c′) 5−2.5 suspension and (d, d′) 2.5−2.5 suspension mechanically stirred at150 rpm. Every sample has two images: the first image captured using a digital camera and the second one using an optical microscope. The photos were taken by one of the authors (Y.B.S.).

0.195 μA cm^{-2} is achieved by the sample coated in the diluted 2.5−2.5 suspension. However, in 5−5 and 5−2.5 suspensions, the i_{corr} values of the coated Mg alloy increase to 1.096 and 1.352 μA cm^{-2}, respectively, which are in agreement with the reverse sequence of EIS results. (iii) As shown in Figure 11a, the cathodic branches are considered to represent the

https://doi.org/10.1021/acsomega.1c05625
ACS Omega 2022, 7, 1021−1034

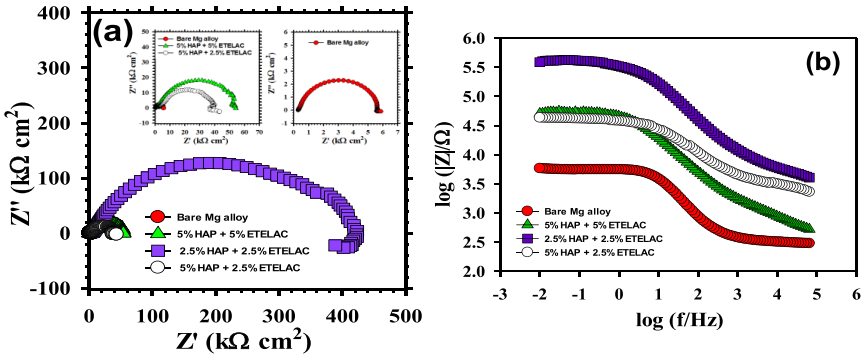

Figure 9. (a) Nyquist and (b) Bode plots measured in SBF at 37 °C for the bare Mg alloy and three coated samples in different suspension concentrations.

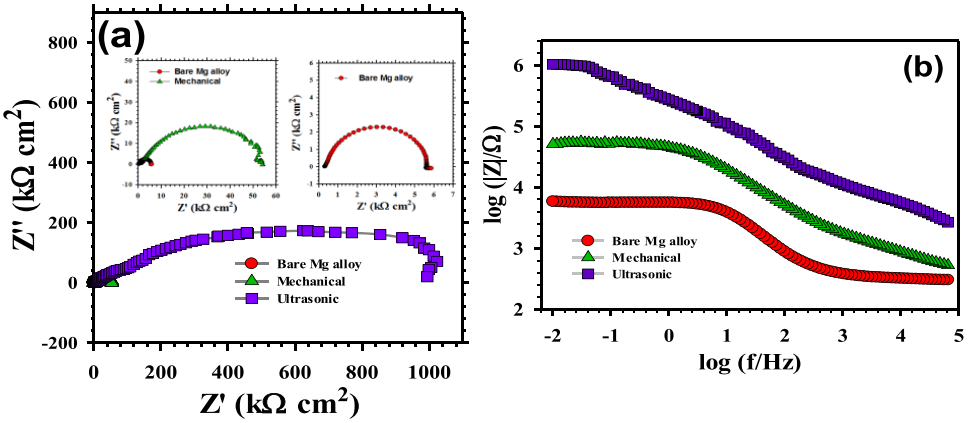

Figure 10. (a) Nyquist and (b) Bode plots measured in SBF at 37 °C for the bare Mg alloy and coated samples in 5% HAP + 5% ETELAC suspension under both ultrasonic and mechanical stirring modes.

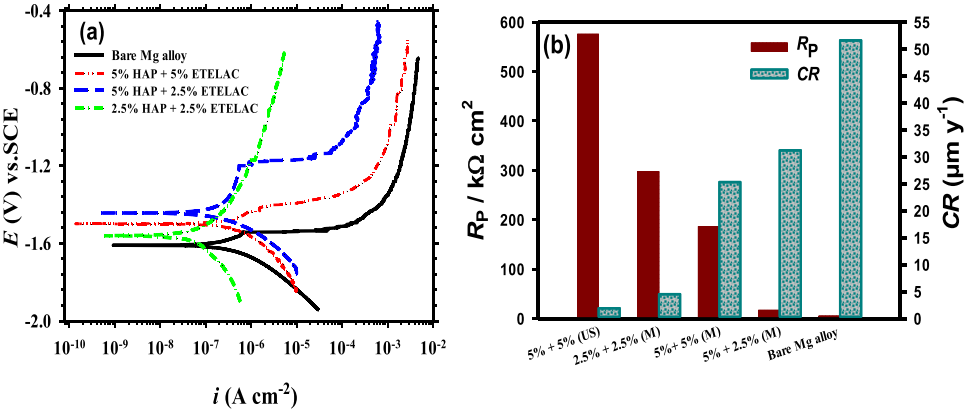

Figure 11. (a) Polarization curves in SBF at 37 °C of the bare Mg alloy and coated alloy samples at 50 V in different suspension concentrations mechanically stirred at 150 rpm. (b) Histograms for the polarization resistance (R_{pol}) and corrosion rate (CR) of the same samples in SBF at 37 °C and the sample coated at 50 V in 5% HAP + 5% ETELAC suspension with ultrasonic (US) stirring.

hydrogen evolution process, while the anodic ones characterize the active dissolution and passivation processes of the alloy.[56−58] (iv) The coated sample in 5−5 suspension showed a lower anodic limiting current, which correlated with that of the bare Mg alloy; however, it shows a slightly more cathodic depolarization effect than the uncoated Mg alloy, probably with a positive shift in the corrosion potential (E_{corr}) toward a more positive value. (v) The coated sample in 5−2.5 suspension exhibits a lower anodic limiting current than that recorded for the one coated in 5−5 suspension and shows a limited region of passivity on its anodic branch. More cathodic depolarization is recorded in the case of the sample coated in 5−5 suspension than that coated in 5−2.5 suspension. Coated samples using 2.5−2.5 suspension showed the lowest anodic and cathodic limiting currents among all tested samples. (vi) It has to be stated that all coated samples have a positive shift in their E_{corr} value compared to the bare Mg alloy (−1.622 V); however, this cannot be taken as a dependable criterion for decreasing their corrosion rate among each other, but the i_{corr} value is the main parameter that validates the corrosion resistance. (v) The average corrosion rate[46] in μm y^{-1} is also

https://doi.org/10.1021/acsomega.1c05625
ACS Omega 2022, 7, 1021−1034

Table 3. Summary of Various Polarization Corrosion Parameters for All Samples in SBF at 37 °C[a]

sample	i_{corr} (μA cm^{-2})	R_{pol} (kΩ cm^2)	b_a (V/dec)	$-b_c$ (V/dec)	CR (μm y^{-1})
bare Mg alloy substrate	2.233	5.278	0.028	0.188	51.02
5% HAP + 5% ETELAC (MS)	1.096	186.20	0.073	0.113	25.04
5% HAP + 5% ETELAC (US)	0.083	575.60	0.168	0.128	1.90
5% HAP + 2.5% ETELAC (MS)	1.352	16.66	0.652	0.174	30.89
2.5% HAP + 2.5% ETELAC (MS)	0.195	297.50	0.151	0.174	4.46

[a](MS) is for a mechanically stirred bath at 150 rpm, and (US) is for an ultrasonically stirred bath.

correlated with i_{corr} in μA cm^{-2} via the following conversion expression:[58]

$$CR = 22.85 i_{corr} \quad (5)$$

Likewise, the polarization resistance (R_{pol}) of all tested samples can be evaluated and is listed in Table 3 based on the Stern−Geary equation[51] (eq 6):

$$R_{pol} = \frac{b_a b_b}{2.303(b_a + b_c)} \times \frac{1}{i_{corr}} \quad (6)$$

(vi) The lowest i_{corr} value is obtained for the sample coated in 2.5−2.5 suspension. This sample exhibits also a quite large passive zone in its anodic branch. (vii) Generally, all coated Mg alloy samples presented a higher R_{pol} value than the bare Mg alloy, likely due to the introduction of the insulator material ETELAC resin. This would confer to the coating with better barrier properties and thus prevent the corrosive medium from reaching the substrate. (vii) Figure 11b illustrates the correlation between the tested samples based on their CR and R_p values. Generally speaking, the effect on Mg alloy fortification by lowering its corrosion rate and enhancing its polarization resistance (R_p in kΩ cm^2) is conducive to the following trend: 5−5 (US) (575.6) > 2.5−2.5 (MS) (297.5) > 5−5 (MS) (186.2) > 5−2.5 (MS) (166.6) > bare Mg alloy (5.278).

Many authors have used the Tafel polarization method in assessing the *in vitro* degradation rates of their tested Mg alloys in various simulated physiological fluids, such as phosphate buffer saline (PBS) and SBF.[59−62] Table 4 compiles some published data concerning the polarization i_{corr} values of Mg alloys coated with HAP in comparison to the obtained value for the coated Mg−3Zn−0.8Ca alloy in the present work. It may be noted that the EPD of nanoHAP/ETELAC composite coating can be a suitable solution for protecting the alloy from degradation in SBF as compared to the other reported works.

Table 4. Comparison of the Corrosion Current Density (i_{corr}) Values of the Coated Mg−3Zn−0.8Ca Alloy with Similar Reported Values for Some Other Mg-Based Alloys Coated with Hydroxyapatite

alloy tested	solution	i_{corr} (μA cm^{-2})
WE43[59]	PBS	43.08
EW10X04[59]	PBS	34.97
EW62[59]	PBS	18.32
AZ91[60]	SBF	0.350
Mg-Zn-Mn[61]	SBF	5.430
AZ31B[62]	SBF	0.387
Mg−3Zn−0.8Ca (present work)	SBF	0.083

CONCLUSIONS

- NanoHAP powder was successfully fabricated via simple hydrothermal microwave-assisted radiation with a crystal size ranging from 38.8 to 79.8 nm as estimated from XRD analysis, which is in good accordance with the HR-TEM results.
- The ETELAC resin dispersing agent can increase the suspension stability of nanoHAP in aqueous solution with no agglomeration for about 1 h. Zeta potential measurement further assures the ability of ETELAC to attain suspension stability.
- For EPD in 5% HAP + 5% ETELAC (5−5) suspension using single-run (S) or double-run deposition experiments (D_5, D_{10}, and D_{20}), the weight gain increased as the applied voltages were increased under stagnant or stirring conditions until a definite value of 30 or 50 V, respectively. Beyond these potential limits, excessive gas evolution adversely affects the morphology and reduces the weight gain of the formed coated layer.
- At each definite voltage, for single S or double D_5 and D_{20} runs, the suspension concentration has a significant effect on the weight gain and coating morphology in a manner that the diluted 2.5% HAP + 2.5% ETELAC (2.5−2.5) suspension always gave the lowest weight gain. This would be conducive to the formation of a thin coating with better barrier properties. For all studied suspensions, a larger weight gain is obtained with the extension of the deposition time of the double runs.
- Under ultrasonic (US) stirring conditions, the weight gain for both S and D_{20} tests was found to be lower than their counterpart runs under mechanical (M) stirring at 150 rpm.
- Electrochemical corrosion behavior assessment using EIS and PDP measurements for the coated samples was performed in SBF at 37 °C and compared to that for the uncoated Mg alloy. The results demonstrate that the propensity of any coating to protect the metallic substrate depends on the suspension used for its preparation, being enhanced in the following order based on the polarization resistance value (R_p in kΩ cm^2) of the coated samples: 5−5 (US) (575.6) > 2.5−2.5 (297.5) > 5−5 (186.2) > 5−2.5 (166.6) > bare Mg alloy (5.278).
- Future work is being performed on the best coating obtained over prolonged time intervals to evaluate its behavior and degradation mechanism in an aggressive environment necessary for its various orthopedic applications.

EXPERIMENTAL SECTION

Preparation of the Alloy Samples. The metallic substrate Mg alloy samples with the composition Mg−3 wt % Zn−0.8 wt % Ca were prepared from pure Mg (99.99%), Zn (99.98%), and Ca (99.98%) by the technical specialists in the manufacturing technology and metal casting department at CMRDI, Cairo, Egypt. Ca and Zn were chosen as alloying

https://doi.org/10.1021/acsomega.1c05625
ACS Omega 2022, 7, 1021−1034

elements as they are both benign and essential elements for the human body. Specimens in a similar cylindrical rod shape with 24 mm diameter were molded from the alloy, and each one was further cut into four equal quarters with 10 cm^2 area each. Before coating, specimens were all abraded progressively with 600, 1000, and 1500 grit SiC papers, washed thoroughly with deionized water (DIW), then ultrasonically cleaned in ethanol for 5 min, and finally dried in warm air. Prior to each EPD experiment, a magnesium fluoride (MgF_2) conversion layer was applied by steeping the sample in 40% HF solution for 1 min at 25 °C, followed by rinsing with DIW, and then was left to dry in air.

Preparation of NanoHAP Powder. NanoHAP powder was prepared using analytical grade reagents and deionized water throughout. Calcium carbonate ($CaCO_3$) as a calcium ion source was from Fluka, disodium hydrogen phosphate anhydrous (Na_2HPO_4) as a phosphate ion source and ethylene diamine tetraacetic acid (EDTA) as a calcium complexing and masking agent were both from Fisher Scientific, and NaOH for adjusting the solution pH was from Sigma-Aldrich. One liter of 0.1 M EDTA as disodium salt solution was prepared with DIW. Since $CaCO_3$ is sparingly soluble in water, an equal molar ratio of $CaCO_3$ was added stepwise to 0.1 M EDTA solution with continuous stirring to achieve a final concentration of 0.1 M Ca-EDTA as a stable complex. While being stirred, 0.06 M Na_2HPO_4 solution was added dropwise until the complete mixing of the final solution to achieve a Ca/P ratio of 1.67. Next, 0.1 M NaOH was used to adjust the pH value of the final solution at 12.8−13.0. The prepared overall solution was then transferred to a microwave oven with an output power of 800 W at 2.45 GHz for 20 min. After complete precipitation, the solution was taken out from the microwave oven and left for cooling and filtration. The precipitate was washed several times with hot DIW to ensure the complete removal of all sodium hydroxide molecules and then dried in an oven at 80 °C for 2 h to obtain a fine powder. The prepared nanoHAP was characterized using the XRD technique (Bruker, Germany). The size and morphology of the synthesized nanoHAP powder were also determined using TEM images. The used transmission electron microscope type was G 20 S Twin, Netherlands.

Electrophoresis Deposition. Fabricated nanoHAP powder was dispersed in a benign resin solution of ETELAC (from HAWKING Electrotechnology Limited, UK) containing 1-methoxy-2-propanol and ethylene glycol monohexyl ether as dispersing agents. Three different suspensions with concentration ratios of 5% HAP + 5% ETELAC, 5% HAP + 2.5% ETELAC, and 2.5% HAP + 2.5% ETELAC were prepared in DIW for the electrophoresis deposition experiment. These three suspensions were selected based on the dispersion physical properties regarding results of agglomeration and zeta potential measurements. The electrophoresis deposition cell was of two-electrode assembly including a hollow circular AISI 316L stainless steel anode and Mg alloy sample as the cathode suspended at its center. A glass cell of 1000 mL capacity was connected to a programmable DC power supply workstation (Chroma, model 62050P-100-100). A magnetic stirrer was used to control the stirring rate of the dispersing medium and a thermometer was used for measuring its temperature. All nanoHAP deposition experiments were performed at room temperature (25 °C), as a higher temperature leads to an increase in ion and particle mobilities in the suspension, which increase the chance for water molecules to reach the two electrodes, causing electrolysis and gas evolution. Raising the temperature could also result in more ionization of water molecules in the solution and, hence, an increase in its ion concentration and conductivity.

Electrochemical Corrosion Tests. Electrochemical impedance spectroscopy (EIS) and potentiodynamic polarization (PDP) tests were performed on the coated samples and bare Mg alloy substrate. All tests were carried out using an AutoLab potentiostat/galvanostat (PGSTAT30) workstation. The PDP curves were recorded at a scan rate of 1 mV/s. The EIS measurements were conducted at the open-circuit potential after 1 h immersion to establish a steady-state value, utilizing an applied perturbation ac signal of 10 mV amplitude over a frequency domain from 100 kHz down to 0.01 Hz. A conventional three-electrode cell with platinum and saturated calomel (SCE) as counter and reference electrodes, respectively, was used. The working electrode was the coated sample with an exposed area of 0.196 cm^2. The test electrolyte solution was simulated body fluid (SBF) with pH 7.4,[25] containing NaCl (8.0 g/L), KCl (0.4 g/L), $CaCl_2$ (0.14 g/L), $NaHCO_3$ (0.35 g/L), $MgSO_4{\cdot}7H_2O$ (0.2 g/L), KH_2PO_4 (0.1 g/L), Na_2HPO_4 (0.06 g/L), and glucose (1.0 g/L). Each experiment was performed at least twice to achieve reproducibility.

■ ASSOCIATED CONTENT

Supporting Information

The Supporting Information is available free of charge at https://pubs.acs.org/doi/10.1021/acsomega.1c05625.

Table S1: weight gain of S experiments at different voltages using 5% HAP + 5% ETELAC suspension without stirring and with stirring at 150 rpm; Table S2: weight gain (in mg/cm^2) at different voltages for the double runs D_5, D_{10}, and D_{20} in 5% HAP + 5% ETELAC suspension without stirring and with stirring at 150 rpm; Table S3: weight gains (in mg/cm^2) at different applied voltages in 5% HAP + 2.5% TELAC and 2.5% HAP + 2.5% ETELAC suspensions with mechanical stirring at 150 rpm (PDF)

■ AUTHOR INFORMATION

Corresponding Author

Fakiha El-Taib Heakal − *Chemistry Department, Faculty of Science, Cairo University, Giza 12613, Egypt*; orcid.org/0000-0002-4398-6194; Email: fakihaheakal@yahoo.com, hfakiha@cu.edu.eg

Authors

Yahia B. Sarhan − *Chemistry Department, Faculty of Science, Cairo University, Giza 12613, Egypt*

Maamoun A. Maamoun − *Central Metallurgical Research and Development Institute (CMRDI), Cairo 12422, Egypt*

Amira M. Bakry − *Chemistry Department, Faculty of Science, Cairo University, Giza 12613, Egypt*; orcid.org/0000-0002-9783-8963

Yasser K. Abdel-Monem − *Chemistry Department, Faculty of Science, Menoufia University, Shebin El-Kom 32511, Egypt*

Ibrahim M. Ghayad − *Central Metallurgical Research and Development Institute (CMRDI), Cairo 12422, Egypt*

Complete contact information is available at: https://pubs.acs.org/10.1021/acsomega.1c05625

https://doi.org/10.1021/acsomega.1c05625
ACS Omega 2022, 7, 1021−1034

Author Contributions

F.E.-T.H. conceived and designed the overall project. Samples were synthesized and characterized by Y.B.S. and M.A.M. Electrochemical measurements were measured and analyzed by Y.B.S., M.A.M., and I.M.G. Drawing and writing of the first draft were done by Y.B.S. and A.M.B. Revision of the draft was made by Y.K.A.-M. and I.M.G.

Notes

The authors declare no competing financial interest.

■ ACKNOWLEDGMENTS

The research supports provided by the Chemistry Department, Faculty of Science, Cairo University, and CMRDI are highly appreciated.

■ REFERENCES

(1) Hao, L.; Dadbakhsh, S.; Seaman, O.; Felstead, M. Selective laser melting of a stainless steel and hydroxyapatite composite for load-bearing implant development. *J. Mater. Process. Technol.* **2009**, *209*, 5793−5801.
(2) Van Noort, R. Titanium: the implant material of today. *J. Mater. Sci.* **1987**, *22*, 3801−3811.
(3) Lopes, M. S.; Jardini, A. L.; Maciel Filho, R. Poly (lactic acid) production for tissue engineering applications. *Procedia Eng.* **2012**, *42*, 1402−1413.
(4) Tan, L.; Yu, X.; Wan, P.; Yang, K. Biodegradable materials for bone repairs: a review. *J. Mater. Sci. Technol.* **2013**, *29*, 503−513.
(5) Hornberger, H.; Virtanen, S.; Boccaccini, A. R. Biomedical coatings on magnesium alloys−a review. *Acta Biomater.* **2012**, *8*, 2442−2455.
(6) Xin, Y.; Hu, T.; Chu, P. K. In vitro studies of biomedical magnesium alloys in a simulated physiological environment: a review. *Acta Biomater.* **2011**, *7*, 1452−1459.
(7) Somekawa, H.; Mukai, T. High strength and fracture toughness balance on the extruded Mg−Ca−Zn alloy. *Mater. Sci. Eng., A* **2007**, *459*, 366−370.
(8) Song, Y.; Han, E.-H.; Shan, D.; Yim, C. D.; You, B. S. The effect of Zn concentration on the corrosion behavior of Mg−xZn alloys. *Corros. Sci.* **2012**, *65*, 322−330.
(9) Tehranchi, A.; Yin, B.; Curtin, W. A. Solute strengthening of basal slip in Mg alloys. *Acta Mater.* **2018**, *151*, 56−66.
(10) Wang, H. X.; Guan, S. K.; Wang, X.; Ren, C. X.; Wang, L. G. In vitro degradation and mechanical integrity of Mg−Zn−Ca alloy coated with Ca-deficient hydroxyapatite by the pulse electro-deposition process. *Acta Biomater.* **2010**, *6*, 1743−1748.
(11) Wang, H.; Guan, S.; Wang, Y.; Liu, H.; Wang, H.; Wang, L.; Ren, C.; Zhu, S.; Chen, K. In vivo degradation behavior of Ca-deficient hydroxyapatite coated Mg−Zn−Ca alloy for bone implant application. *Colloids Surf., B* **2011**, *88*, 254−259.
(12) Gitiara, A.; Tabaian, S. H. Corrosion Behavior of Mg−Zn−Ca−Mn Alloy Coated with Nano-hydroxyapatite by Cyclic Voltammetry Method. *J. Bio- Tribo- corros.* **2021**, *7*, 45−16.
(13) Wang, Y.; Li, X.; Chen, M.; Zhao, Y.; You, C.; Li, Y.; Chen, G. In vitro and in vivo degradation behavior and biocompatibility evaluation of microarc oxidation-fluoridated hydroxyapatite-coated Mg−Zn−Zr−Sr alloy for bone application. *ACS Biomater. Sci. Eng.* **2019**, *5*, 2858−2876.
(14) Sivakumar, M.; Manjubala, I. Preparation of hydroxyapatite/fluoroapatite-zirconia composites using Indian corals for biomedical applications. *Mater. Lett.* **2001**, *50*, 199−205.
(15) Singh, S.; Singh, G.; Bala, N. Corrosion behavior and characterization of HA/Fe_3O_4/CS composite coatings on AZ91 Mg alloy by electrophoretic deposition. *Mater. Chem. Phys.* **2019**, *237*, 121884.
(16) Büyüksağiş, A.; Çiftçi, N. HAP Coatings for Biomedical Applications: Biocompatibility and Surface Protection Against Corrosion of Ti, Ti6Al4V and AISI 316L SS. *Prot. Met. Phys. Chem. Surf.* **2020**, *56*, 834−843.
(17) Aegerter, M. A.; Jafelicci, M., Jr.; Souza, D. F.; Zanotto, E. D. Sol-gel fibers and coating films. *Sol Gel Sci. Technol. World Sci. Singapore* 1989 *XX*, pp. 346−374, DOI: 10.1142/9789814541312.
(18) Cao, N.; Dong, J.; Wang, Q.; Ma, Q.; Xue, C.; Li, M. An experimental bone defect healing with hydroxyapatite coating plasma sprayed on carbon/carbon composite implants. *Surf. Coat. Technol.* **2010**, *205*, 1150−1156.
(19) Mattox, D. Film Formation, Adhesion, Surface Preparation and Contamination Control. *de Handbook of Physical Vapor Deposition (PVD) Processing*; Park Ridge: New Jersey, 1998.
(20) Liu, X.; Chu, P. K.; Ding, C. Formation of apatite on hydrogenated amorphous silicon (a-Si: H) film deposited by plasma-enhanced chemical vapor deposition. *Mater. Chem. Phys.* **2007**, *101*, 124−128.
(21) Besra, L.; Liu, M. A review on fundamentals and applications of electrophoretic deposition (EPD). *Prog. Mater. Sci.* **2007**, *52*, 1−61.
(22) Safavi, M. S.; Walsh, F. C.; Surmeneva, M. A.; Surmenev, R. A.; Khalil-Allafi, J. Electrodeposited hydroxyapatite-based biocoatings: Recent progress and future challenges. *Coatings* **2021**, *11*, 110.
(23) Heakal, F. E.-T.; Shoeib, M. A.; Maanoum, M. A. Optimizing parameters affecting electroless Ni-P coatings on AZ91D magnesium alloy as corrosion protection barriers. *Prot. Met. Phys. Chem. Surf.* **2017**, *53*, 177−187.
(24) Heakal, F. E.-T.; Tantawy, N.; Shehata, O. Impact of chloride and fluoride additions on surface reactivity and passivity of AM60 magnesium alloy in buffer solution. *Corros. Sci.* **2012**, *64*, 153−163.
(25) Song, G. Control of biodegradation of biocompatable magnesium alloys. *Corros. Sci.* **2007**, *49*, 1696−1701.
(26) Viswanath, B.; Shastry, V.; Ramamurty, U.; Ravishankar, N. Effect of calcium deficiency on the mechanical properties of hydroxyapatite crystals. *Acta Mater.* **2010**, *58*, 4841−4848.
(27) Suchanek, K.; Bartkowiak, A.; Gdowik, A.; Perzanowski, M.; Kąc, S.; Szaraniec, B.; Suchanek, M.; Marszałek, M. Crystalline hydroxyapatite coatings synthesized under hydrothermal conditions on modified titanium substrates. *Mater. Sci. Eng. C.* **2015**, *51*, 57−63.
(28) Liu, J.; Li, K.; Wang, H.; Zhu, M.; Xu, H.; Yan, H. Self-assembly of hydroxyapatite nanostructures by microwave irradiation. *Nanotechnology* **2005**, *16*, 82.
(29) Tamai, H.; Yasuda, H. Preparation of polymer particles coated with hydroxyapatite. *J. Colloid Interface Sci.* **1999**, *212*, 585−588.
(30) Pu'ad, N. M.; Koshy, P.; Abdullah, H. Z.; Idris, M.; Lee, T. C. Syntheses of hydroxyapatite from natural sources. *Heliyon* **2019**, *5*, No. e01588.
(31) Kappe, C. Microwave Assisted Extraction of Benzofurane Derivative from Petasites Hybridus Rhizomes. *Angew. Chem. Int. Ed.* **2004**, *43*, 6256.
(32) Ji, X.-J.; Cheng, Q.; Wang, J.; Zhao, Y.-B.; Han, Z.-Z.; Zhang, F.; Li, S.-Q.; Zeng, R.-C.; Wang, Z.-L. Corrosion resistance and antibacterial effects of hydroxyapatite coating induced by polyacrylic acid and gentamicin sulfate on magnesium alloy. *Front. Mater. Sci.* **2019**, *13*, 87−98.
(33) Fernando, M. S.; de Silva, R. M.; Nalin de Silva, K. M. Synthesis, characterization, and application of nano hydroxyapatite and nanocomposite of hydroxyapatite with granular activated carbon for the removal of Pb^{2+} from aqueous solutions. *Appl. Surf. Sci.* **2015**, *351*, 95−103.
(34) Holzwarth, U.; Gibson, N. The Scherrer equation versus the 'Debye-Scherrer equation'. *Nat. Nanotechnol.* **2011**, *6*, 534−534.
(35) Mahmoudizadeh, M.; Irankhah, A.; Irankhah, R. A performance study on the electrocoating process with a CuZnAl nanocatalyst for a methanol steam reformer: the effect of time and voltage. *RSC Adv.* **2016**, *6*, 25934−25942.
(36) Krüger, H.; Knote, A.; Schindler, U.; Kern, H.; Boccaccini, A. Composite ceramic-metal coatings by means of combined electrophoretic deposition and galvanic methods. *J. Mater. Sci.* **2004**, *39*, 839−844.

https://doi.org/10.1021/acsomega.1c05625
ACS Omega 2022, 7, 1021−1034

(37) Cho, J.; Konopka, K.; Rożniatowski, K.; García-Lecina, E.; Shaffer, M. S. P.; Boccaccini, A. R. Characterisation of carbon nanotube films deposited by electrophoretic deposition. *Carbon* **2009**, *47*, 58−67.
(38) Zhitomirsky, I.; Gal-Or, L. Electrophoretic deposition of hydroxyapatite. *J. Mater. Sci. Mater. Med.* **1997**, *8*, 213−219.
(39) Javidi, M.; Javadpour, S.; Bahrololoom, M. E.; Ma, J. Electrophoretic deposition of natural hydroxyapatite on medical grade 316L stainless steel. *Mater. Sci. Eng. C.* **2008**, *28*, 1509−1515.
(40) Zhitomirsky, I. Electrophoretic and electrolytic deposition of ceramic coatings on carbon fibers. *J. Eur. Ceram. Soc.* **1998**, *18*, 849−856.
(41) Pishbin, F.; Simchi, A.; Ryan, M. P.; Boccaccini, A. R. Electrophoretic deposition of chitosan/45S5 Bioglass® composite coatings for orthopaedic applications. *Surf. Coat. Technol.* **2011**, *205*, 5260−5268.
(42) Hanh, H. D.; Dong, N. T.; Starvarache, C.; Okitsu, K.; Maeda, Y.; Nishimura, R. Methanolysis of triolein by low frequency ultrasonic irradiation. *Energy convers. manage.* **2008**, *49*, 276−280.
(43) Yui, T.; Mori, Y.; Tsuchino, T.; Itoh, T.; Hattori, T.; Fukushima, Y.; Takagi, K. Synthesis of photofunctional titania nanosheets by electrophoretic deposition. *Chem. Mater.* **2005**, *17*, 206−211.
(44) Santillán, M. J.; Membrives, F.; Quaranta, N.; Boccaccini, A. R. Characterization of TiO_2 nanoparticle suspensions for electrophoretic deposition. *J. Nanopart. Res.* **2008**, *10*, 787−793.
(45) Radice, S.; Mischler, S.; Michler, J. Threshold value of particle concentration in epd: Experimental evidence with Tio2 organic suspensions. In *Key Eng. Mater*; 2009; Trans Tech Publ: Vol. *412*, pp 51−56.
(46) Radice, S.; Bradbury, C. R.; Michler, J.; Mischler, S. Critical particle concentration in electrophoretic deposition. *J. Eur. Ceram. Soc.* **2010**, *30*, 1079−1088.
(47) Bakhsheshi-Rad, H. R.; Hamzah, E.; Fereidouni-Lotfabadi, A. H. A.; Daroonparvar, M.; Yajid, M. A. M.; Mezbahul-Islam, M.; Kasiri-Asgarani, M.; Medraj, M. Microstructure and bio-corrosion behavior of Mg−Zn and Mg−Zn−Ca alloys for biomedical applications. *Mater. Corros.* **2014**, *65*, 1178−1187.
(48) Maleki, E.; Shahri, F.; Emamy, M. Microstructure and Tensile Properties of Mg−5Zn Alloy Containing Ca. *Met. Mater. Int.* **2021**, *27*, 1565−1577.
(49) Lakshmi, R. V.; Basu, B. J. Fabrication of superhydrophobic sol−gel composite films using hydrophobically modified colloidal zinc hydroxide. *J. Colloid Interface Sci.* **2009**, *339*, 454−460.
(50) Magdaleno-López, C.; de Jesús Pérez-Bueno, J. Quantitative evaluation for the ASTM D4541-17/D7234 and ASTM D3359 adhesion norms with digital optical microscopy for surface modifications with flame and APPJ. *Int. J. Adhes/ Adhes/* **2020**, *98*, 102551.
(51) Heakal, F. E.-T.; Bakry, A. M. Corrosion degradation of AXJ530 magnesium alloy in simulated pysiological fluid and its mitigation by fluoride and chitosan coatings for osteosynthetic applications. *Int. J. Electrochem. Sci.* **2018**, *13*, 7724−7747.
(52) Heakal, F. E.-T.; Bakry, A. M. Electrochemical Characterization of Certain Mg-Based Alloys in Artificial Perspiration Biofluid for Consumer and Industrial Applications. *J. Mater. Eng. Perform.* **2019**, *28*, 4379−4392.
(53) Brusciotti, F.; Snihirova, D. V.; Xue, H.; Montemor, M. F.; Lamaka, S. V.; Ferreira, M. G. Hybrid epoxy−silane coatings for improved corrosion protection of Mg alloy. *Corros. Sci.* **2013**, *67*, 82−90.
(54) Astm, G. *Standard practice for calculation of corrosion rates and related information from electrochemical measurements*; G102−89, 2004.
(55) Chiu, K. Y.; Wong, M. H.; Cheng, F. T.; Man, H. C. Characterization and corrosion studies of fluoride conversion coating on degradable Mg implants. *Surf. Coat. Technol.* **2007**, *202*, 590−598.
(56) Heakal, F. E.-T.; Bakry, A. M. Role of amoxicillin in enhancing AZ31 alloy degradation resistance and its monitoring using nano-Pd electrochemical sensor. *Mater. Chem. Phys.* **2019**, *234*, 224−236.
(57) Chang, J.-W.; Guo, X.-W.; Fu, P.-H.; Peng, L.-M.; Ding, W.-J. Effect of heat treatment on corrosion and electrochemical behaviour of Mg−3Nd−0.2 Zn−0.4 Zr (wt.%) alloy. *Electrochim. Acta* **2007**, *52*, 3160−3167.
(58) Heakal, F. E.-T.; Bakry, A. M. Serum albumin can influence magnesium alloy degradation in simulated blood plasma for cardiovascular stenting. *Mater. Chem. Phys.* **2018**, *220*, 35−49.
(59) Dunne, C. F.; Levy, G. K.; Hakimi, O.; Aghion, E.; Twomey, B.; Stanton, K. T. Corrosion behaviour of biodegradable magnesium alloys with hydroxyapatite coatings. *Surf. Coat. Technol.* **2016**, *289*, 37−44.
(60) Mukhametkaliyev, T. M.; Surmeneva, M. A.; Vladescu, A.; Cotrut, C. M.; Braic, M.; Dinu, M.; Vranceanu, M. D.; Pana, I.; Mueller, M.; Surmenev, R. A. A biodegradable AZ91 magnesium alloy coated with a thin nanostructured hydroxyapatite for improving the corrosion resistance. *Mater. Sci. Eng. C.* **2017**, *75*, 95−103.
(61) Prakash, C.; Singh, S.; Pabla, B. S.; Uddin, M. S. Synthesis, characterization, corrosion and bioactivity investigation of nano-HA coating deposited on biodegradable Mg-Zn-Mn alloy. *Surf. Coat. Technol.* **2018**, *346*, 9−18.
(62) Yu, W.; Sun, R.; Guo, Z.; Wang, Z.; He, Y.; Lu, G.; Chen, P.; Chen, K. Novel fluoridated hydroxyapatite/MAO composite coating on AZ31B magnesium alloy for biomedical application. *Appl. Surf. Sci.* **2019**, *464*, 708−715.

https://doi.org/10.1021/acsomega.1c05625
ACS Omega 2022, 7, 1021−1034